



**QUEEN'S  
UNIVERSITY  
BELFAST**

## Spatially resolved steady-state negative capacitance

Yadav, A. K., Nguyen, K. X., Hong, Z., García-Fernández, P., Aguado-Puente, P., Nelson, C. T., Das, S., Prasad, B., Kwon, D., Cheema, S., Khan, A. I., Hu, C., Iñiguez, J., Junquera, J., Chen, L. Q., Muller, D. A., Ramesh, R., & Salahuddin, S. (2019). Spatially resolved steady-state negative capacitance. *Nature*, 565(7740), 468-471. <https://doi.org/10.1038/s41586-018-0855-y>

**Published in:**  
Nature

**Document Version:**  
Peer reviewed version

**Queen's University Belfast - Research Portal:**  
[Link to publication record in Queen's University Belfast Research Portal](#)

### **Publisher rights**

© 2019 Springer Nature Limited. This work is made available online in accordance with the publisher's policies. Please refer to any applicable terms of use of the publisher.

### **General rights**

Copyright for the publications made accessible via the Queen's University Belfast Research Portal is retained by the author(s) and / or other copyright owners and it is a condition of accessing these publications that users recognise and abide by the legal requirements associated with these rights.

### **Take down policy**

The Research Portal is Queen's institutional repository that provides access to Queen's research output. Every effort has been made to ensure that content in the Research Portal does not infringe any person's rights, or applicable UK laws. If you discover content in the Research Portal that you believe breaches copyright or violates any law, please contact [openaccess@qub.ac.uk](mailto:openaccess@qub.ac.uk).

### **Open Access**

This research has been made openly available by Queen's academics and its Open Research team. We would love to hear how access to this research benefits you. – Share your feedback with us: <http://go.qub.ac.uk/oa-feedback>

## **Spatially Resolved Steady State Negative Capacitance**

Ajay K. Yadav<sup>1\*</sup>, Kayla X. Nguyen<sup>2\*</sup>, Zijian Hong<sup>3\*</sup>, Pablo García-Fernández<sup>4\*</sup>, Pablo Aguado-Puente<sup>5</sup>, Christopher T. Nelson<sup>6,7</sup>, Sujit Das<sup>7</sup>, Bhagawati Prasad<sup>7</sup>, Daewoong Kwon<sup>1</sup>, Suraj Cheema<sup>7</sup>, Asif I. Khan<sup>1,⊥</sup>, Jorge Íñiguez<sup>8</sup>, Javier Junquera<sup>4</sup>, Long-Qing Chen<sup>3</sup>, David A. Muller<sup>9,10</sup>, Ramamoorthy Ramesh<sup>7</sup>, Sayeef Salahuddin<sup>1</sup>

<sup>1</sup>Department of Electrical Engineering and Computer Sciences, University of California, Berkeley, CA 94720, USA

<sup>2</sup>Department of Chemistry and Chemical Biology, Cornell University, Ithaca, New York, NY 14853, USA

<sup>3</sup>Department of Materials Science and Engineering, Pennsylvania State University, State College, PA 16802, USA

<sup>4</sup>Departamento de Ciencias de la Tierra y Física de la Materia Condensada, Universidad de Cantabria, Cantabria Campus Internacional, 39005 Santander, Spain

<sup>5</sup>Atomistic Simulation Center, Queen's University Belfast, Belfast BT7 1NN, United Kingdom

<sup>6</sup>National Center for Electron Microscopy, Lawrence Berkeley Laboratory, Berkeley, CA 94720, USA

<sup>7</sup>Department of Materials Science and Engineering, University of California, Berkeley, CA 94720, USA

<sup>8</sup>Materials Research and Technology Department, Luxembourg Institute of Science and Technology, L-4362 Esch/Alzette, Luxembourg

<sup>9</sup>Kavli Institute at Cornell for Nanoscale Science, Cornell University, Ithaca, New York, NY 14853, USA

<sup>10</sup>Kavli Institute at Cornell for Nanoscale Science, Cornell University, Ithaca, New York,  
NY 14853, USA

<sup>⊥</sup> present address: School of Electrical and Computer Engineering, Georgia Institute of  
Technology, GA 30332

\*These authors contributed equally to this work

Negative capacitance is a new state of ferroelectric materials that promises to revolutionize modern day electronics by exploiting a region of thermodynamic space that is normally not accessible<sup>1-14</sup>. While existing reports of negative capacitance clearly substantiate the importance of this phenomenon, they have been focused on its macroscopic manifestation. These macroscopic manifestations demonstrate the implication of steady state negative capacitance, e.g. by enhancing the capacitance of a ferroelectric-dielectric heterostructure<sup>4,7,14</sup> or by improving the subthreshold swing of a transistor<sup>8-12</sup>. Yet, they constitute only indirect measurements of the local state of negative capacitance at which the ferroelectric resides. A spatial mapping of this phenomenon is thus critical for a microscopic understanding, and for the optimal design of devices with potential technological applications. Here we demonstrate a direct measurement of the *steady state negative capacitance* in a ferroelectric-dielectric heterostructure. We use electron microscopy complemented with phase-field and second-principles simulations in SrTiO<sub>3</sub>/PbTiO<sub>3</sub> (STO/PTO) superlattices, to directly determine, with atomic resolution, the local regions in the ferroelectric material where a state of negative capacitance is stabilized. Simultaneous vector mapping of atomic displacements (related with a complex pattern of vortices in the polarization field), in conjunction with reconstruction of the local electric field identify the negative capacitance region as those with higher energy density and larger polarizability: the domain walls where the polarization is suppressed.

When a material transitions to a ferroelectric phase, it develops a stable polarization state which is doubly degenerate<sup>1</sup> (Fig. 1a), corresponding to positions of minima ('A' and 'B' in Fig. 1a) in its free energy landscape,  $G^1$ . At these stable states, the curvature of the free energy is positive, *i.e.*

$\frac{\partial^2 G}{\partial D^2} > 0$ , indicating positive permittivity ( $\epsilon \propto [\frac{\partial^2 G}{\partial D^2}]^{-1}$ ), where  $D$  is the electric displacement field.

These equilibrium states are separated by a region where the curvature is negative ( $\frac{\partial^2 G}{\partial D^2} < 0$ ), defining a region of negative permittivity (highlighted as the region between H-K in Fig. 1a,b<sup>2</sup>. It is possible to stabilize the ferroelectric in this negative permittivity region, by adding the parabolic energy landscape of a normal dielectric (Fig. 1b) to the double-well structure of the ferroelectric. Accessing such “forbidden” regions of the thermodynamic landscape of ferroic materials at equilibrium remains a grand challenge in condensed matter physics. In addition to providing key insights into fascinating fundamental physics, such a steady state negative capacitance has profound implications for lowering the energy consumption in conventional electronics, *i.e.*, the Boltzmann Tyranny<sup>2,5</sup>. However, the exploration of negative capacitance has been constrained by the thermodynamic requirement that, in a physical system, the capacitance is always positive – which meant the emergence of negative capacitance could only be probed indirectly, through an observation of capacitance enhancement<sup>4,7,14</sup>. In order to directly probe the state of negative capacitance, one would need to measure the polarization and electric fields internal to the material locally. In addition, the ‘double-well’ concept described above is only representative of a single domain scenario. So it is important to examine how this will change in presence of domains<sup>14-15</sup>. Here, we use STO/PTO superlattices as a model system that breaks into vortex like domains<sup>16-18</sup>. Remarkably, we find the emergence of local regions of negative capacitance at the domain walls where the polarization is suppressed. In addition, we find that these walls are also the regions where the energy density is larger than that in the bulk of the domains where the polarization is not suppressed, from which one can infer a negative curvature of ( $\frac{\partial^2 G}{\partial D^2} < 0$ ), in close resemblance to the ‘double well’ model. This is shown schematically in Fig. 1(c).

We use the superlattices of SrTiO<sub>3</sub>/PbTiO<sub>3</sub> as our model Ferroelectric-Dielectric heterostructure system where a state of negative capacitance is expected to be stabilized in the

equilibrium. In such superlattices vortex-like topologies<sup>16-18</sup> are observed as the dominant polarization pattern when the periodicity is optimal<sup>19-21</sup>. The defining characteristic of these topologies is the gradual suppression of polarization near the center of the vortex. Occurrence of such vortex structures in a displacive ferroelectric such as  $\text{PbTiO}_3$  enables us to perform detailed measurements of the local configuration of the polarization using Scanning Transmission Electron Microscopy (STEM) techniques<sup>22-24</sup>. For a  $(\text{SrTiO}_3)_{12}/(\text{PbTiO}_3)_{12}$  superlattice, polar atomic displacement vectors ( $\mathbf{P}_{\text{PD}}$ ) when extracted from atomic-resolution STEM images<sup>19,23-25</sup> reveal stabilization of a well-defined array of clockwise and anti-clockwise rotating polarization patterns (Fig. 2a). The spatial variation of the polarization along the horizontal and vertical axes is shown in Fig. 2b,c. The suppression of polarization near the vortex core becomes more apparent when a 2D map of the magnitude ( $|\mathbf{P}_{\text{PD}}|$ ) is plotted (Fig. 2d), corresponding to the polarization region detailed in Fig. 2a). In these regions of suppressed polarization, we expect the material to be in a relatively high energy state, which suggests that these vortex cores should exhibit negative permittivity.

To test this hypothesis, we utilized STEM in conjunction with the newly developed electron microscopy pixel array detector (EMPAD)<sup>24</sup> which records the full momentum distribution at every scan position, providing sufficient information to simultaneously measure the polar order and electric field. Here, convergent beam electron diffraction (CBED) mapping of the probability current flow ( $\langle p \rangle$ ) of conjugate disks, (200)/(-200) and (020)/(0-20), quantitatively measures the polarization field (Fig. 3a) in a  $12 \times 12$   $\text{SrTiO}_3/\text{PbTiO}_3$  superlattice<sup>24</sup> (described in detail in Supplementary section B). The polarization field reproduces the same vortex structures (Fig. 3a) as the ones obtained by an independent, Z-contrast, HRSTEM technique (Fig. 2a). To reconstruct the macroscopic electric field (Fig. 3b), we note that the average electric field,  $E(r_0)$ <sup>28</sup>

is equal to the average field over the volume of the crystal cell ‘ $V_c$ ’ that contains the lattice point  $r_0$ :

$$E(r_0) = \frac{1}{V_c} \int dV e(r) \quad (1)$$

, where ‘ $e(r)$ ’ is microscopic field defined to be the nuclear field of the atom, and ‘ $dV$ ’ is the volume over which the polarity is measured (see supplementary section B for details).

Our technique is the most robust away from the interfaces as it is the least affected by offsets there. Therefore, we focus on the line A-B in Fig. 2a which goes through the middle of the ferroelectric layer. Also, along this line the  $x$  component of the polarization and electric field is negligible and thus we can simply look at the  $z$  components. Fig. 3c shows the experimentally measured,  $z$ -component of the polarization ( $P_z$ ) and electric field ( $E_z$ ) along this line. The magnitude of the measured polarization was calibrated using the spontaneous polarization of PTO<sup>29</sup>. Notice how the polarization changes from full-length up to full-length down through regions of suppressed polarization including zero. This then allows us to relate the  $E_z$ , which in this case is really the internal field ( $E_{int}$ ) (as there is no externally applied bias), as a function of  $P_z$ . We note here that the extraction of this functional dependence is an approximation (a local relation is assumed). However, this approximation is well justified by the fact that if we look into individual vortices, the  $E_z$  vs  $P_z$  dependence remains similar within the experimental resolution. We next find the displacement from  $D_z = \epsilon_0 E_z + P_z$  and the free energy  $G$  from  $G \approx \int E_z dD_z$  (see supplementary section E and Fig. S7a,b for details). This estimated  $G$  as a function of  $D_z$  shows a clear negative curvature  $\frac{\partial^2 G}{\partial D^2} < 0$  near the regions where  $D_z$  is small. Therefore, the spatial mapping of the polarization and the electric field shows local regions of the ferroelectric stabilized in a state where  $\frac{\partial^2 G}{\partial D^2}$  is estimated to be negative. We can further correlate the values of  $D_z$  according to its

occurrence along the x direction. This gives a mapping of the local energy densities along the x direction as shown in Fig. 3d. Note how the shape and amplitude of the energy density function looks very similar from core to core. Based on this analysis, we would expect that local regions of negative permittivity will appear in the regions at and near the core. We cannot do a direct measurement of this fact as EMPAD measurements cannot be done in presence of externally applied field currently. Nonetheless, considering the fact that, in a capacitor measurement, the externally applied bias would be very small, it is possible to estimate permittivity near the core, assuming this external bias to be a small perturbation. Fig. S8 shows permittivity estimated in this manner and indeed, we find negative permittivity around the core (See Supplementary section F for details). These estimations from the experimental measurement are validated by both phase-field and second-principles calculations where it is possible to apply a field and directly calculate the response function. As shown in Fig. 4b,d, the permittivity is found to be negative in the regions near the core. Furthermore, a full two dimensional mapping of the local energy densities calculated from second principles, shown in Supplementary Fig S6, demonstrates that this negative permittivity appears at the regions of higher energy density, exactly as it is estimated from the experiment in Fig. 3d. Finally, for a self-consistent check, we have measured the macroscopic capacitance of these superlattices. Indeed, compared to the capacitance of the constituent STO, the superlattice shows a 3.7X enhancement in the capacitance, a hall mark of stabilization of the ferroelectric layer at the state of negative capacitance (see Supplementary section G and Fig. S9).

The details of the calculations performed using phase-field and second-principles methods have been provided in Supplementary sections C, D and E respectively. Extended Data Fig. S3 shows detailed polarization and electric field vector-maps from the phase field calculations. In



accordance with Fig. 3, in Fig. 4a, we have plotted the  $z$  components of polarization ( $P_z$ ) and electric field ( $E_z$ ) along a line that goes through the cores of the vortices. The behavior of both ' $P_z$ ' and ' $E_z$ ' strongly resembles the experimental data in Fig. 3c. A similar conclusion is arrived at from the second principles *ab initio* calculations in Fig. 4c,d where polarization and electric field vectors along the core were plotted from the full 2D map of the polarization and electric field vectors.

It is important to note that the change in polarization always aligns with the *external field*, i.e., the  $\partial P / \partial E_{\text{external}}$  or the conventional susceptibility is always positive, even locally. This is shown in Fig. S5b. Note how the local susceptibility is always positive even in the regions where the permittivity itself is negative. In fact regions of negative permittivity arise where the susceptibility becomes very large, i.e., where the material becomes highly polarizable. This is also discussed in the Supplementary section F, where we show that the estimation of permittivity from the experimental data becomes negative only when the polarizability is very high.

An important aspect of our work is the simultaneous mapping of both the polarity<sup>19</sup> and the electric field<sup>24</sup> inside the polarization vortices. This is what makes it possible to estimate the local energy density and therefore the local permittivity. Only mapping out the local polarization<sup>30-33</sup> would not be enough to probe local permittivity. It is also important to note that the vortices lead to a full rotation of the polarization from up to down within just 4 nm (see Fig. 2a and 3c). As a result the volume of the domain wall, where the polarization is suppressed, for vortices is significantly enhanced compared to conventional 180° domains. Thus vortices are highly conducive to negative capacitance. Nonetheless, vortices are not necessary to observe negative capacitance. A key insight that can be gained from this work is that, in a multi-domain system, the negative capacitance ensues

from the domain walls<sup>14</sup> and it should be possible to control its strength by engineering the energetics of the system that increases/decreases the size of the domain wall. In this vein the superlattice structure that we used is an example but bi-layer, tri-layer or any combination of ferroelectric-dielectric heterostructure is equally applicable. A recent theoretical study<sup>34</sup> has shown how negative capacitance may be stabilized in the nano domains in a ferroelectric thin film. In the same context, systems with mixed Bloch-Néel domain walls<sup>35</sup> could be relevant. Further work should also investigate improper ferroelectrics<sup>36</sup> where polarization is not the order parameter.

In summary, we report the observation of steady state arrays of negative capacitance in epitaxial superlattices comprised of ferroelectric PTO and non-ferroelectric STO. The polarization in the PTO layer accommodates the competition between elastic and electrostatic energies by forming arrays of clockwise and counter-clockwise vortex-like structures. The core of such vortices displays regions of suppressed polarization and larger energy densities where the total change in the internal field dominates over the change in the external field<sup>37</sup>, making the curvature  $\frac{\partial^2 G}{\partial D^2}$  negative. The fact that two different theoretical models can reproduce the experimental observation indicates that such stabilization in the ‘forbidden’ region of the thermodynamic landscape should be amenable to predictive material design. One further remarkable observation is the fact that the superlattice forms a periodic array of negative and positive capacitance states, pointing to the intriguing possibility of new types of metamaterials.

## References

1. Lines, M. E. & Glass, A. M. Principles and Applications of Ferroelectrics and Related Materials. (Oxford University Press, 2001).
2. S. Salahuddin and S. Datta, "Use of negative capacitance to provide voltage amplification for low power nanoscale devices," *Nano Lett.*, vol. 8, no. 2, pp. 405–410, 2008.
3. S. Salahuddin and S. Datta, "Can the subthreshold swing in a classical fet be lowered below 60 mV/decade?," in *Electron Devices Meeting, 2008. IEDM 2008. IEEE International*, pp. 1–4, IEEE, 2008.
4. A. I. Khan, D. Bhowmik, P. Yu, S. J. Kim, X. Pan, R. Ramesh, and S. Salahuddin, "Experimental evidence of ferroelectric negative capacitance in nanoscale heterostructures," *Appl. Phys. Lett.*, vol. 99, no. 11, p. 113501, 2011.
5. T. N. Theis and P. M. Solomon, "It's time to reinvent the transistor!," *Science*, vol. 327, no. 5973, pp. 1600–1601, 2010.
6. W. Gao, A. Khan, X. Marti, C. Nelson, C. Serrao, J. Ravichandran, R. Ramesh, and S. Salahuddin, "Room-temperature negative capacitance in a ferroelectric–dielectric superlattice heterostructure," *Nano Lett.*, vol. 14, no. 10, pp. 5814–5819, 2014.
7. D. J. Appleby, N. K. Ponon, K. S. Kwa, B. Zou, P. K. Petrov, T. Wang, N. M. Alford, and A. O'Neill, "Experimental observation of negative capacitance in ferroelectrics at room temperature," *Nano Lett.*, vol. 14, no. 7, pp. 3864–3868, 2014.
8. A. Rusu, G. Salvatore, D. Jimenez, and A. M. Ionescu, "Metal-ferroelectric-meta-oxide-semiconductor field effect transistor with sub-60mV/decade subthreshold swing and internal voltage amplification," in *Electron Devices Meeting (IEDM), 2010, IEEE International*, pp. 16–3, 2010.
9. K.-S. Li, P.-G. Chen, T.-Y. Lai, C.-H. Lin, C.-C. Cheng, C.-C. Chen, Y.-J. Wei, Y.-F. Hou, M.-H. Liao, M.-H. Lee, *et al.*, "Sub-60mV-swing negative-capacitance finfet without hysteresis," in *2015 IEEE International Electron Devices Meeting, (IEDM)*, pp. 22–6, IEEE, 2015.
10. Z. Krivokapic, U. Rana, R. Galatage, A. Razavieh, A. Aziz, J. Liu, J. Shi, H. Kim, R. Sporer, C. Serrao, *et al.*, "14nm ferroelectric finfet technology with steep subthreshold slope for ultra low power applications," in *Electron Devices Meeting (IEDM), 2017 IEEE International*, pp. 15–1, IEEE, 2017.
11. J. Jo and C. Shin, "Negative capacitance field effect transistor with hysteresis-free sub-60-mV/decade switching," *IEEE Electron Device Letters*, vol. 37, no. 3, pp. 245–248, 2016.
12. D. Kwon, K. Chatterjee, A. J. Tan, A. K. Yadav, H. Zhou, A. B. Sachid, R. Dos Reis, C. Hu, and S. Salahuddin, "Improved subthreshold swing and short channel effect in fdsoi n-channel

negative capacitance field effect transistors,” *IEEE Electron Device Letters*, vol. 39, no. 2, pp. 300–303, 2018.

13. Khan, A. I. et al. Negative capacitance in a ferroelectric capacitor. *Nat Mater* 14, 182-186, doi:10.1038/nmat4148<http://www.nature.com/nmat/journal/v14/n2/abs/nmat4148.html> - [supplementary-information](http://www.nature.com/nmat/journal/v14/n2/abs/nmat4148.html) (2015).

14. Zubko, P. et al. Negative capacitance in multidomain ferroelectric superlattices. *Nature* 534, 524-528, doi:10.1038/nature17659

<http://www.nature.com/nature/journal/v534/n7608/abs/nature17659.html> - [supplementary-information](http://www.nature.com/nature/journal/v534/n7608/abs/nature17659.html) (2016).

15 Cano, A., and D. Jiménez. "Multidomain ferroelectricity as a limiting factor for voltage amplification in ferroelectric field-effect transistors." *Applied Physics Letters* 97.13 (2010): 133509.

16 Karpov, D. et al. Three-dimensional imaging of vortex structure in a ferroelectric nanoparticle driven by an electric field. *Nature Communications* 8, 280, doi:10.1038/s41467-017-00318-9 (2017).

17 Wang, J., Kamlah, M., Zhang, T.-Y., Li, Y. & Chen, L.-Q. Size-dependent polarization distribution in ferroelectric nanostructures: Phase field simulations. *Applied Physics Letters* 92, 162905, doi:doi:<http://dx.doi.org/10.1063/1.2917715> (2008).

18 Naumov, I. I., Bellaiche, L. & Fu, H. Unusual phase transitions in ferroelectric nanodisks and nanorods. *Nature* 432, 737-740 (2004).

19 Yadav, A. K. et al. Observation of polar vortices in oxide superlattices. *Nature* 530, 198-201, doi:10.1038/nature16463 (2016).

20 Hong, Z. et al. Stability of Polar Vortex Lattice in Ferroelectric Superlattices. *Nano letters* 17, 2246-2252, doi:10.1021/acs.nanolett.6b04875 (2017).

21 Damodaran, A. R. et al. Phase coexistence and electric-field control of toroidal order in oxide superlattices. *Nat Mater* advance online publication, doi:10.1038/nmat4951

<http://www.nature.com/nmat/journal/vaop/ncurrent/abs/nmat4951.html> - [supplementary-information](http://www.nature.com/nmat/journal/vaop/ncurrent/abs/nmat4951.html) (2017).

22 Urban, K. W. Studying Atomic Structures by Aberration-Corrected Transmission Electron Microscopy. *Science* 321, 506 (2008).

23 Jia, C.-L. et al. Unit-cell scale mapping of ferroelectricity and tetragonality in epitaxial ultrathin ferroelectric films. *Nat Mater* 6, 64-69, doi:[http://www.nature.com/nmat/journal/v6/n1/suppinfo/nmat1808\\_S1.html](http://www.nature.com/nmat/journal/v6/n1/suppinfo/nmat1808_S1.html) (2007).

- 24 Nguyen, K. X. et al. Reconstruction of Polarization Vortices by Diffraction Mapping of Ferroelectric  $\text{PbTiO}_3$  /  $\text{SrTiO}_3$  Superlattice Using a High Dynamic Range Pixelated Detector. *Microscopy and Microanalysis* 22, 472-473, doi:10.1017/S1431927616003214 (2016).
- 25 Nelson, C. T. et al. Spontaneous Vortex Nanodomain Arrays at Ferroelectric Heterointerfaces. *Nano letters* 11, 828-834, doi:10.1021/nl1041808 (2011).
- 26 Tang, Y. L. et al. Atomic-scale mapping of dipole frustration at  $90^\circ$  charged domain walls in ferroelectric  $\text{PbTiO}_3$  films. 4, 4115, doi:10.1038/srep04115 (2014).
- 27 Tang, Y. L. et al. Observation of a periodic array of flux-closure quadrants in strained ferroelectric  $\text{PbTiO}_3$  films. *Science* 348, 547-551, doi:10.1126/science.1259869 (2015).
- 28 Kittel, C. *Introduction to solid state physics*. (Wiley, 1966).
- 29 Watanabe, Y. in *Ferroelectric Thin Films: Basic Properties and Device Physics for Memory Applications* (eds Masanori Professor Okuyama & Yoshihiro Ishibashi) 177-199 (Springer Berlin Heidelberg, 2005).
- 30 Qi, Y., Chen, Z., Huang, C., Wang, L., Han, X., Wang, J., ... & Chen, L. (2012). Coexistence of ferroelectric vortex domains and charged domain walls in epitaxial  $\text{BiFeO}_3$  film on (110)  $\text{O GdScO}_3$  substrate. *Journal of Applied Physics*, 111(10), 104117.
- 31 Lee, M. H., C-P. Chang, F-T. Huang, G. Y. Guo, B. Gao, C. H. Chen, S-W. Cheong, and M-W. Chu. "Hidden Antipolar Order Parameter and Entangled Néel-Type Charged Domain Walls in Hybrid Improper Ferroelectrics." *Physical review letters* 119, no. 15 (2017): 157601.
- 32 Zhang, Qinghua, Guotai Tan, Lin Gu, Yuan Yao, Changqing Jin, Yanguo Wang, Xiaofeng Duan, and Richeng Yu. "Direct observation of multiferroic vortex domains in  $\text{YMnO}_3$ ." *Scientific reports* 3 (2013): 2741.
- 33 Gruverman, Alexei, D. Wu, H. J. Fan, I. Vrejoiu, M. Alexe, R. J. Harrison, and J. F. Scott. "Vortex ferroelectric domains." *Journal of Physics: Condensed Matter* 20, no. 34 (2008): 342201.
- 34 Sluka, Tomas, Pavel Mokry, and Nava Setter. "Static negative capacitance of a ferroelectric nano-domain nucleus." *Applied Physics Letters* 111, no. 15 (2017): 152902.
- 35 Lee, Donghwa, Rakesh K. Behera, Pingping Wu, Haixuan Xu, Y. L. Li, Susan B. Sinnott, Simon R. Phillpot, L. Q. Chen, and Venkatraman Gopalan. "Mixed Bloch-Néel-Ising character of  $180^\circ$  ferroelectric domain walls." *Physical Review B* 80, no. 6 (2009): 060102.
- 36 Bousquet, Eric, Matthew Dawber, Nicolas Stucki, Celine Lichtensteiger, Patrick Hermet, Stefano Gariglio, Jean-Marc Triscone, and Philippe Ghosez. "Improper ferroelectricity in perovskite oxide artificial superlattices." *Nature* 452, no. 7188 (2008): 732.
- 37 Chang, S. C., Avci, U. E., Nikonov, D. E., & Young, I. A. (2017). A thermodynamic perspective of negative-capacitance field-effect transistors. *IEEE Journal on Exploratory Solid-State Computational Devices and Circuits*, 3, 56-64.



**Acknowledgements** This work was supported in part by the AFOSR YIP program, the LEAST (one of the SRC/DARPA supported centers within the STARNET initiative), the Berkeley Center for Negative Capacitance Transistors. Electron microscopy experiments and equipment supported by the Cornell Center for Materials Research, through the National Science Foundation MRSEC program, award #DMR 1719875. The work at Penn State is supported by U.S. Department of Energy, Office of Basic Energy Sciences, Division of Materials Sciences and Engineering under Award FG02-07ER46417. Z.J.H acknowledges the support by NSF-MRSEC grant number DMR-1420620 and NSF-MWN grant number DMR-1210588. R.R. acknowledges support from the Moore Foundation and funding from the Army Research Office. J.I. acknowledges support from the Luxembourg National Research Fund under grant C15/MS/10458889 NEWALLS. P.G.F. and J.J. acknowledge financial support from the Spanish Ministry of Economy and Competitiveness through grant number FIS2015-64886-C5-2-P, and P.G.F. acknowledges support from Ramón y Cajal grant No. RyC-2013-12515. .

**Author Contributions** A.K.Y., K.N., D.A.M., R.R, and S.S. designed research. A.K.Y. performed synthesis and characterization of superlattice films. K.N. performed polarization and electric field measurements on superlattice films using EMPAD-STEM. C.T.N. performed atomic-resolution polar displacement mapping on superlattice films using STEM. Z.H. and L.Q.C. performed Phase-Field calculations for these superlattice structures. P.G.F., P.A.P., J.I. and J.J. performed Second-Principles calculations for these superlattice structures. A.K.Y., S.S., R.R., K.N., C.T.N, A.I.K., Z.H., P.G.F., P.A.P., J.J., L.Q.C., D.A.M, J.I. co-wrote the manuscript. SS performed the overall supervision of the work. All authors contributed to the discussions and manuscript preparation.

**Author Information** Reprints and permissions information is available at [www.nature.com/reprints](http://www.nature.com/reprints). The authors declare no competing financial interests. Readers are welcome to comment on the online version of the paper. Correspondence and requests for materials should be addressed to sayeef@berkeley.edu

## Figures Legends

**Figure 1 | Steady State of Negative Capacitance:** Free energy landscape for a ferroelectric material is shown in **a**. Free energy landscape for a ferroelectric/dielectric heterostructure is shown in **b**. **Energy density in a multi-domain system juxtaposed with the variation of polarization** is shown in **c**. **The domain walls where the polarization is suppressed have more energy density than the bulk domain.**

**Figure 2 | Identifying the regions of negative permittivity.** Overlay of polarization vector map (indicated by the cyan vectors) on a cross sectional HAADF STEM image of a PTO layer embedded within a  $(\text{SrTiO}_3)_{12}/(\text{PbTiO}_3)_{12}$  superlattice is shown in **a**. Variation in  $x$ - and  $z$ -components of polarization ( $P_x$  and  $P_z$  respectively) along a horizontal line (A-B) passing through the core of vortices is shown in **b**. Line profiles showing the variation in  $x$ - and  $z$ -components of polarization ( $P_x$  and  $P_z$  respectively) along two vertical lines C-D and E-F passing through the core of the vortices is shown in **c**. Two-dimensional color map showing the variation in magnitude of polar displacements (for the same sub-region shown in Fig. 2a) with an overlay of polarization vector map (indicated by black vectors) is shown in **d**.



**Figure 3 | Measurement of local electric field and polarization field using EMPAD-STEM.**

Polarization vector map from a sub-region of PTO layer embedded with a  $(\text{SrTiO}_3)_{12}/(\text{PbTiO}_3)_{12}$  superlattice as measured using STEM (details in Methods, Extended Data Fig. 1 and 2) is shown in **a**. Local electric field in a PTO layer (corresponding to the same region shown in Fig. 3a) as measured using TEM is shown **b**. Variation in  $z$ -components of local polarization ( $P_z$ ) and electric field ( $E_z$ ) along a horizontal line (indicated by green dotted line in Fig. 3a and b) which passes through the core of vortices is shown in **c**. Local energy density estimated from the variation of ( $P_z$ ) and electric field ( $E_z$ ) along the same line. Regions around the core show a negative curvature ( $\frac{\partial^2 G}{\partial D^2} < 0$ ). See details in Supplementary section (E and F).

**Figure 4 | Local dielectric constant calculated using second principles and phase field simulations.**

Phase field simulations and second principles were performed for a  $(\text{SrTiO}_3)_n/(\text{PbTiO}_3)_n$  superlattice to obtain local polarization and electric field distributions within ferroelectric and dielectric layers of the superlattice structure. Polarization pattern from both second principles ( $n=10$ ) and phase field simulations ( $n=12$ ) show the presence of vortex topologies. The variation in  $z$ -components of local polarization,  $P_z$ , (denoted by diamond) and electric field,  $E_z$ , (denoted by circle) predicted from phase field simulations (along a horizontal line which passes through the core of the vortices) is shown in **a** (see Methods and Extended Data Fig. 3). Corresponding variation in  $z$ -component of local dielectric constant ( $\epsilon_{zz}$ ) extracted from local  $P_z$  and  $E_z$  predicted from phase-field simulations is shown in **b** (see Methods). Similarly, a variation in  $z$ -components of local polarization and electric field ( $P_z$  and  $E_z$ ), and extracted dielectric constant ( $\epsilon_{zz}$ ) using second principles calculations is shown in **c** and **d** respectively.



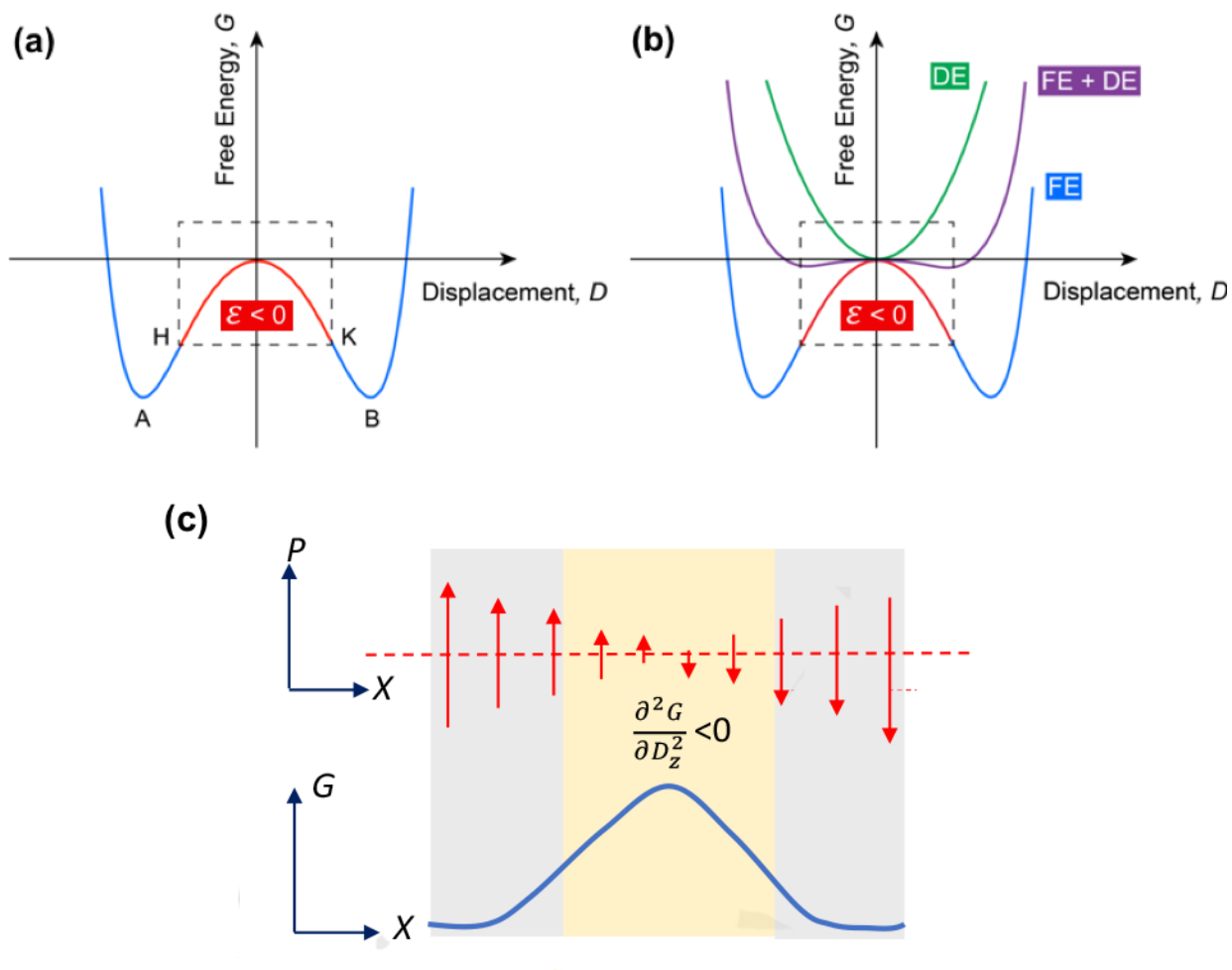


Fig. 1

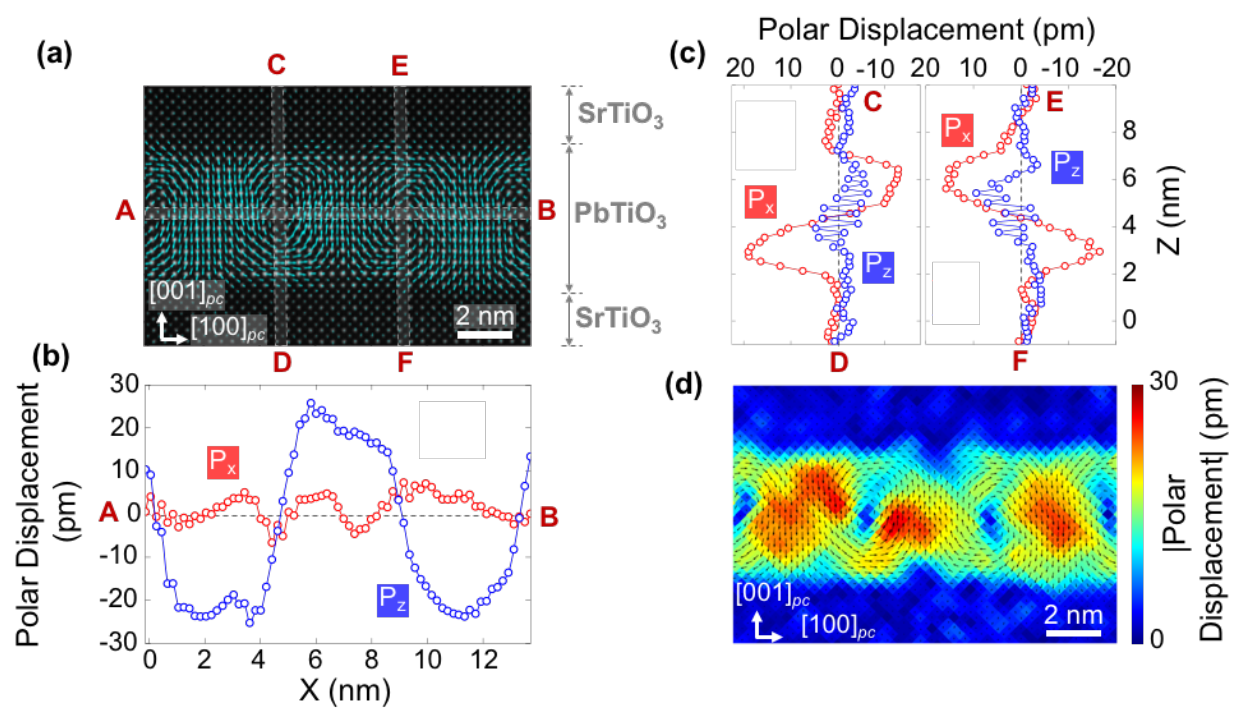


Fig. 2

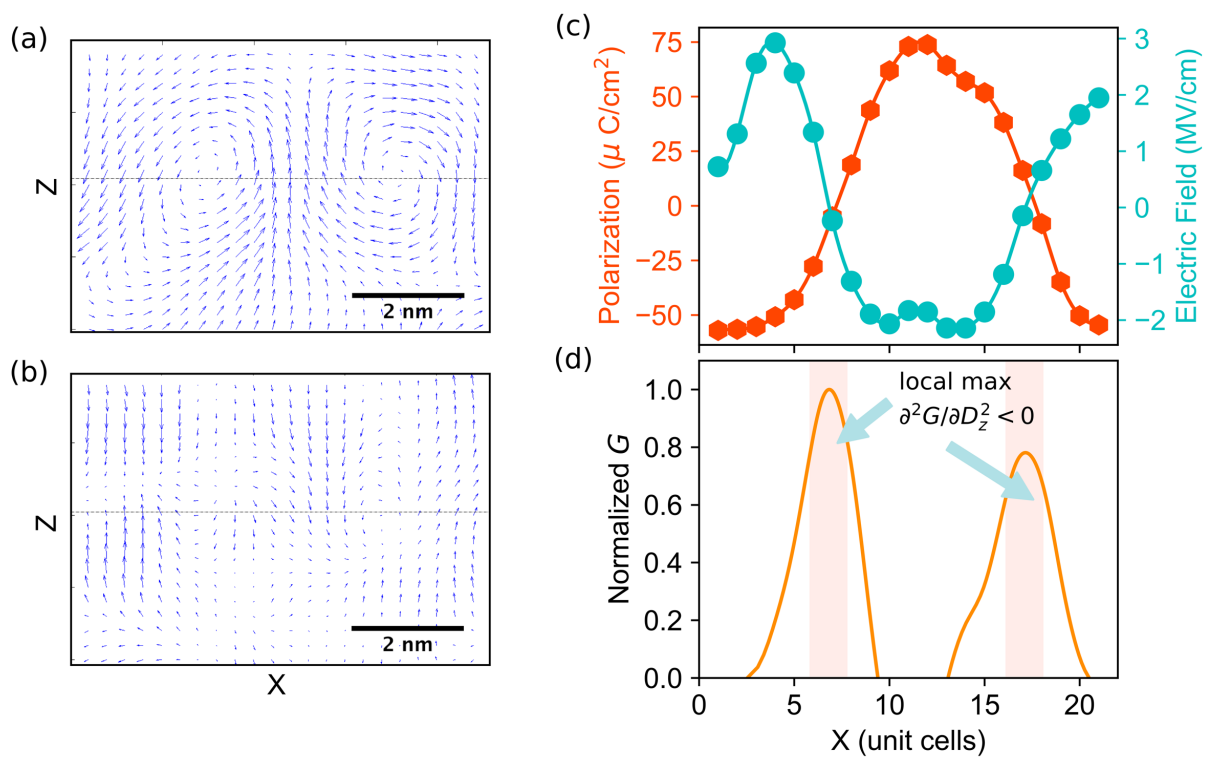


Fig.3

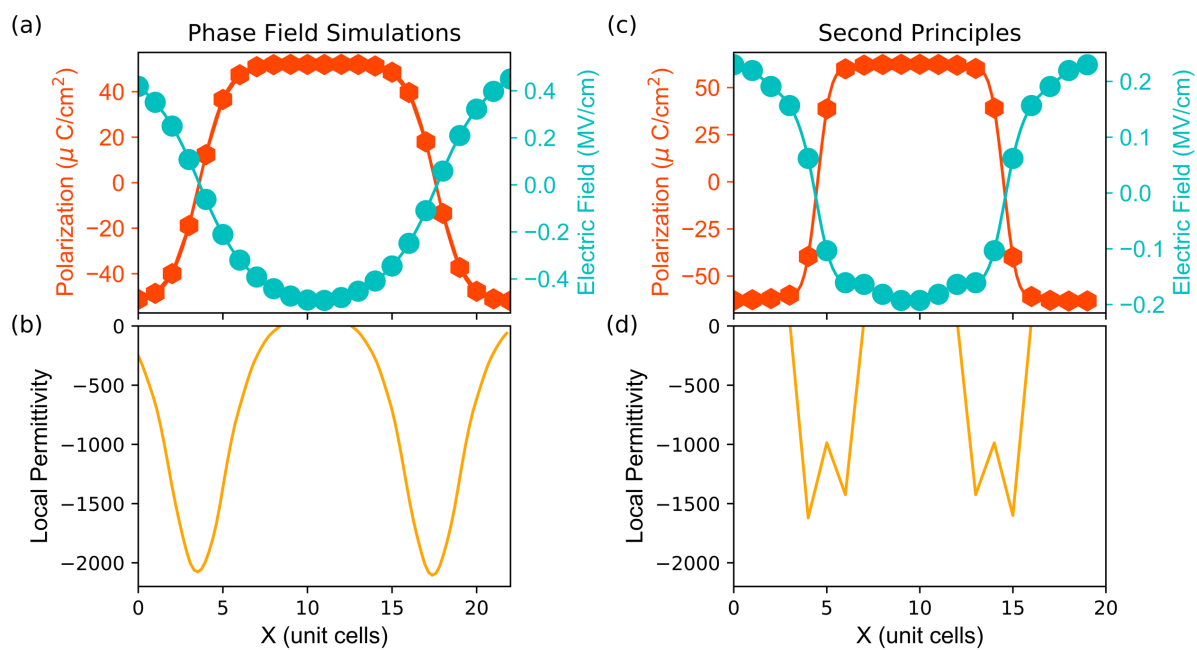


Fig.4.